









# Modelling high-resolution ALMA observations of strongly lensed dusty star-forming galaxies detected by *Herschel*

Jacob Maresca <sup>1</sup>★, Simon Dye <sup>1</sup>, Aristeidis Amvrosiadis,<sup>2</sup> George Bendo <sup>3</sup>, Asantha Cooray,<sup>4</sup> Gianfranco De Zotti,<sup>5</sup> Loretta Dunne,<sup>6</sup> Stephen Eales,<sup>6</sup> Cristina Furlanetto <sup>7</sup>, Joaquin González-Nuevo <sup>8,9</sup>, Michael Greener <sup>1</sup>, Robert Ivison <sup>10</sup>, Andrea Lapi,<sup>11</sup> Mattia Negrello,<sup>6</sup> Dominik Riechers,<sup>12</sup> Stephen Serjeant <sup>13</sup>, Mónica Tergolina<sup>7</sup> and Julie Wardlow<sup>14</sup>

<sup>1</sup>*School of Physics & Astronomy, University of Nottingham, University Park, Nottingham NG7 2RD, UK*

<sup>2</sup>*Centre for Extragalactic Astronomy, Durham University, Department of Physics, South Road, Durham DH1 3LE, UK*

<sup>3</sup>*UK ALMA Regional Centre Node, Jodrell Bank Centre for Astrophysics, Department of Physics and Astronomy, University of Manchester, Oxford Road, Manchester M13 9PL, UK*

<sup>4</sup>*Department of Physics & Astronomy, University of California, Irvine, CA 92697, USA*

<sup>5</sup>*INAF–Osservatorio Astronomico di Padova, Vicolo dell’Osservatorio 5, I-35122 Padova, Italy*

<sup>6</sup>*School of Physics and Astronomy, Cardiff University, Queens Buildings, The Parade, Cardiff CF24 3AA, UK*

<sup>7</sup>*Instituto de Física, Universidade Federal do Rio Grande do Sul, Av. Bento Gonçalves, 9500, 91501-970, Porto Alegre, Brazil*

<sup>8</sup>*Departamento de Física, Universidad de Oviedo, C. Federico Garcia Lorca 18, E-33007 Oviedo, Spain*

<sup>9</sup>*Instituto Universitario de Ciencias y Tecnologías Espaciales de Asturias (ICTEA), C. Independencia 13, E-33004 Oviedo, Spain*

<sup>10</sup>*European Southern Observatory, Karl-Schwarzschild-Strasse 2, D-85748 Garching bei München, Germany*

<sup>11</sup>*SISSA, Via Bonomea 265, I-34136 Trieste, Italy*

<sup>12</sup>*I. Physikalisches Institut, Universität zu Köln, Zùlpicher Strasse 77, D-50937 Köln, Germany*

<sup>13</sup>*Department of Physical Sciences, The Open University, Walton Hall, Milton Keynes MK7 6AA, UK*

<sup>14</sup>*Department of Physics, Lancaster University, Lancaster, LA1 4YB, UK*

Accepted 2022 February 28. Received 2022 February 28; in original form 2021 November 18

## ABSTRACT

We present modelling of  $\sim 0.1$  arcsec resolution Atacama Large Millimetre/submillimetre Array imaging of seven strong gravitationally lensed galaxies detected by the *Herschel* Space Observatory. Four of these systems are galaxy–galaxy strong lenses, with the remaining three being group-scale lenses. Through careful modelling of visibilities, we infer the mass profiles of the lensing galaxies and by determining the magnification factors, we investigate the intrinsic properties and morphologies of the lensed submillimetre sources. We find that these submillimetre sources all have ratios of star formation rate to dust mass that are consistent with, or in excess of, the mean ratio for high-redshift submillimetre galaxies and low redshift ultra-luminous infrared galaxies. Reconstructions of the background sources reveal that the majority of our sample display disturbed morphologies. The majority of our lens models have mass density slopes close to isothermal, but some systems show significant differences.

**Key words:** gravitational lensing; strong – galaxies; structure.

## 1 INTRODUCTION

Submillimetre (submm) galaxies (SMGs; see Casey, Narayanan & Cooray 2014; Blain et al. 2002, for a review) play host to some of the most intense rates of star formation in the Universe. Commonly, the rest-frame UV radiation emitted by their newly formed stars is almost entirely absorbed and re-radiated at submm wavelengths by high-opacity dust (see e.g. Dudzeviciute et al. 2020) produced by low-/intermediate-mass stars and supernovae. SMGs contribute an estimated 20 per cent of the cosmic star formation rate (SFR) density up to a redshift of  $z \sim 4$  (Swinbank et al. 2013; Lapi et al. 2011) and hence provide valuable aid to our understanding of the formation of galaxies during this period.

SMGs also play a key role in our overall picture of galaxy evolution. Similarities in their size, number density, and clustering properties with quiescent galaxies at low redshifts (e.g. Simpson et al. 2014; Toft et al. 2014) is suggestive of an evolutionary connection (An et al. 2019; Dudzeviciute et al. 2020). An explanation for how the population of SMGs became the red and dead population of massive elliptical galaxies observed in the local Universe is underpinned by the process of gas quenching and the mechanism of gas-poor mergers (Oogi & Habe 2012; Guo & White 2008; Lapi et al. 2018). Although considerably less abundant, Ultra Luminous Infrared Galaxies (ULIRGs) found in the local Universe are often seen as analogues to high-redshift SMGs due to their strongly dust-obscured UV luminosities, high infrared luminosities, and comparable bolometric luminosities (Alaghband-Zadeh et al. 2012; Rowlands et al. 2014), and as such ULIRGs can provide useful insight into the processes at play in SMGs.

\* E-mail: [Jacob.Maresca@nottingham.ac.uk](mailto:Jacob.Maresca@nottingham.ac.uk)

The study of high-redshift submm galaxies has benefited greatly from the advent of large interferometric arrays such as the Atacama Large Millimeter/Submillimetre Array (ALMA) (Wootten & Thompson 2009), which allow observations to reach resolutions of  $<0.1$  arcsec and thus probe previously unreachable physical scales. Strong gravitational lensing provides a further boost in spatial resolution due to the magnification of the background source, which is typically within the range of 5–10 for SMGs (Spilker et al. 2016; Bussmann et al. 2013; Bussmann et al. 2015). In addition, there exists a strong lensing bias in the submm regime due to the steep number counts of submm galaxies and the conservation of surface brightness by gravitational lensing. Magnifying this population leads to an increase in the surface density of galaxies above a given flux threshold, making it possible to find lensed sources in wide surveys with a simple cut in flux density above 100 mJy at 500  $\mu\text{m}$  (Blain 1996; Negrello et al. 2007, 2010; Perrotta et al. 2003). Using this technique, follow-up ALMA observations of strongly lensed submm galaxies detected in wide area surveys, such as the Herschel Astrophysical Terahertz Large Area Survey (H-ATLAS; Eales et al. 2010), the Herschel Multi-tiered Extragalactic Survey (HerMES; Oliver et al. 2012), and the Herschel String 82 Survey (HerS; Viero et al. 2014), carried out using the Herschel Space Observatory (Pilbratt et al. 2010), as well as the submm surveys conducted by the Planck satellite (Cañameras et al. 2015) and the millimetre surveys of the South Pole Telescope (Carlstrom et al. 2011) have contributed to a rapidly increasing understanding of galaxy formation in its early stages (Dye et al. 2018; Sun et al. 2021; Harrington et al. 2021; Cañameras et al. 2017a,b). Most existing observations have mainly targeted extremely luminous sources, but with the increased sensitivity of instruments such as ALMA, it has become possible to investigate more typical main-sequence star-forming galaxies that are responsible for the bulk of the Universe's star formation at  $z \sim 3$ .

As samples of known strongly lensed submm galaxies increase in size, so does our range of redshifts at which they have been observed (Wang et al. 2007; Riechers et al. 2013). This is largely thanks to a very negative  $K$ -correction, such that high-redshift galaxies have approximately constant brightness in the submm regime between redshifts  $z \sim 1$ –8 (Blain et al. 2002). Higher redshift sources tend to be lensed by higher redshift lenses due to the scaling of the lensing cross-section with redshift (Turner, Ostriker & Gott 1984). Increasing the redshift range then allows us to study the mass profiles of lenses at earlier epochs, when galaxy evolution is more rapid and less well understood (Dye et al. 2014; Negrello et al. 2014).

High-resolution submm follow-up observations of lensed SMGs not only allow for more precise determination of the lens mass distribution, but also allow intrinsic properties of the source – such as its luminosity, SFR, and gas and dust mass – to be better characterized. Indeed, investigating properties such as these will be the main motivation of this paper. A classic example of this approach is the lensed system SDP.81, first discovered within the H-ATLAS sample and then observed with ALMA (Negrello et al. 2010; ALMA Partnership et al. 2015; Dye et al. 2015; Rybak et al. 2015a; Rybak et al. 2015b). Studies of the molecular gas and dust in lensed submm galaxies constrain models of star formation in the early Universe (Dye et al. 2022; Cava et al. 2018; Dessauges-Zavadsky et al. 2019). Recent studies have begun to reveal the compact nature of dust in SMGs (Puglisi et al. 2019; Tadaki et al. 2020) that indicate a disparity in size when compared with local ULIRGs.

Reconstruction of the background lensed source from interferometer observations can be achieved with two distinct approaches. There are methods that model the visibilities directly in the uv-plane

(Bussmann et al. 2012; Bussmann et al. 2013; Dye et al. 2018), and those that model the cleaned image plane data (Dye et al. 2015; Inoue et al. 2016; Yang et al. 2019b). The benefit of working in the image plane is that the task is significantly less computationally expensive; however, due to the incomplete coverage of the uv-plane, spatially correlated noise is introduced which can in principle bias the inferred lens model. Working directly with the visibility data avoids this problem, at the cost of longer modelling times.

In this work, we carry out lens modelling in the uv-plane of seven galaxies observed with ALMA. Four of these systems are galaxy–galaxy scale, and the remaining three are group-scale lenses. These systems were originally detected by *Herschel* within H-ATLAS and the extension to the HerMES field, HerMES Large Mode Survey (HeLMS; Asboth et al. 2016; Nayyeri et al. 2016). We investigate the intrinsic source properties, namely, their luminosities, SFRs, and gas and dust masses by determining the magnification factors. Additionally, we investigate the morphologies of the reconstructed sources.

The layout of this paper is as follows. Section 2 describes the ALMA observations and other sources that were drawn upon for this work. Section 3 details the methodology of our lens modelling, and Section 4 presents the results of our work. In Section 5, we compare our results to other similar studies. Finally, in Section 6 we summarize our findings and discuss their interpretation. Throughout this paper, we assume a flat  $\Lambda$ CDM cosmology using the 2015 Planck results (Planck Collaboration et al. 2016), with Hubble constant  $H_0 = 67.7 \text{ km s}^{-1} \text{ Mpc}^{-1}$  and matter density parameter  $\Omega_m = 0.307$ .

## 2 DATA

The seven ALMA observations modelled in this work are from the ALMA programme 2013.1.00358.S (PI: Stephen Eales) and are described in detail within Amvrosiadis et al. (2018). The observation targets for the original ALMA programme were selected from the H-ATLAS and HeLMS surveys for having the brightest 500  $\mu\text{m}$  flux densities ( $> \sim 130$  mJy) and with spectroscopic redshifts  $> 1$ , with the exception of HeLMS J235331.9+031718. Originally, 42 sources were identified in this way, but only 16 had follow-up ALMA observations and were selected based on having accessible RAs. Of the 16 sources observed during ALMA cycle 2, 14 exhibit obvious lensing features. Six of these remaining 14 sources have already been modelled in the work of Dye et al. (2018), and are all galaxy–galaxy scale lenses; one of them we leave for future work (Amvrosiadis et al. (in prep.)), and the remaining seven are modelled in this work. Due to the timings of when the ALMA observations were carried out, it was natural to split the sample, leading to all the group scale lenses being dealt with in this paper. Of these seven sources, one was identified in H-ATLAS, whilst the remaining six are from HeLMS.

The spectral set-up employed by ALMA was identical for each of the lensing systems observed. The band 7 continuum observations, comprised of four spectral windows, each with a width of 1875 MHz and centred on the frequencies 336.5, 338.5, 348.5, and 350.5 GHz. The central frequency of 343.404 GHz corresponds to a wavelength of 873  $\mu\text{m}$ . Each spectral window consists of 128 frequency channels, resulting in a spectral resolution of 15.6 MHz. The ALMA configuration utilized between thirty-five and forty-two 12 m antennae, with an on-source integration time of approximately 125 s. Upon combining all four spectral windows, this achieves an angular resolution of 0.12 arcsec and RMS values of approximately 230  $\mu\text{Jy beam}^{-1}$  and 130  $\mu\text{Jy beam}^{-1}$  for the H-ATLAS and HeLMS sources, respectively. This set-up was chosen to optimize band seven continuum observations, as well as to achieve the angular resolutions

**Table 1.** A summary of the targeted position of each source, the number of antennae used in each observation, the continuum sensitivity, the size of the beam, and the physical scale probed at the source redshift.

Short name	Targeted position (RA DEC)	$N_{\text{ant}}$	Sensitivity (mJy beam $^{-1}$ )	$\theta_{\text{maj}} \times \theta_{\text{min}}$ (arcsec $^2$ )	Physical scale (kpc)
G09v1.97	08:30:51.040 +01:32:25.000	35	0.1044	0.229 arcsec $\times$ 0.154 arcsec	1.33
HELMS18	00:51:59.450 +06:22:40.400	42	0.1007	0.187 arcsec $\times$ 0.158 arcsec	1.48
HELMS5	23:40:51.520 –04:19:38.400	46	0.1034	0.229 arcsec $\times$ 0.151 arcsec	1.37
HELMS7	23:24:39.420 –04:39:34.500	46	0.1034	0.218 arcsec $\times$ 0.151 arcsec	1.51
HELMS2	23:32:55.500 –03:11:36.400	46	0.1034	0.227 arcsec $\times$ 0.151 arcsec	1.48
HELMS15	23:32:55.510 –05:34:26.500	46	0.1034	0.223 arcsec $\times$ 0.151 arcsec	1.52
HELMS40	23:53:31.990 +03:17:18.400	42	0.1147	0.260 arcsec $\times$ 0.150 arcsec	1.55–1.33

necessary to probe the interstellar medium on the scales of giant molecular clouds with high signal-to-noise ratio. The synthesized beam shape for HeLMS J005159.4+062240 is the least elliptical of our sample, with a ratio of major to minor axis of  $\sim 1.2$ . For the observation of HeLMS J235331.9+031718, the ratio of major to minor axis of the synthesized beam is the most elliptical of our sample at  $\sim 1.7$ , with the remaining observations having ratios of  $\sim 1.5$ . The maximum recoverable scales for our observations are between 1.32 arcsec and 1.46 arcsec. The details of the number of antennae, achieved sensitivity, and beam sizes are summarized in Table 1.

In this work, we used the visibility data provided by the ALMA science archive, and re-calibrated them using COMMON ASTRONOMY SOFTWARE APPLICATIONS version (CASA) 4.3.1 (McMullin et al. 2007), and the scripts provided by the archive. Baselines flagged as bad by the ALMA data reduction pipeline were excluded from the analysis. The CASA task `tclean` was used to create images in order to measure the flux density of the sources at 873  $\mu\text{m}$ . The images were constructed using a natural weighting scheme and were primary beam corrected. In order to ensure the minor axis of the primary beam was well sampled, image pixel scales of 0.02 arcsec and 0.03 arcsec were used for the H-ATLAS and HeLMS sources, respectively. The data reduction follows closely the method of Dye et al. (2018), with the exception of using natural weighting in favour of Briggs weighting when creating images with `tclean`, in order to provide increased sensitivity for extended sources. Natural weighting, where the visibilities are weighted according to the data weights, provides the highest signal-to-noise ratio and sensitivity, but the poorest resolution. Uniform weighting, where visibilities in more poorly sampled regions of the uv-plane are given greater weighting, achieves better resolution but at the cost of the poorest signal-to-noise ratio and worse reproduction of large-scale emission. Briggs weighting allows for a smoothly varying compromise between natural and uniform weighting, with the extent to which it resembles either method controlled by the ‘robustness’ parameter (Briggs 1995).

For the calculation of intrinsic source properties, photometry from our ALMA data was used in combination with a number of other data sets. Submm photometry, obtained by the *Herschel* Space Observatory, was employed. This photometry made use of two different instruments: the Spectral and Photometric Imaging Receiver (SPIRE; Griffin et al. 2010) at wavelengths of 250, 350, and 500  $\mu\text{m}$ ; and the Photoconductor Array Camera and Spectrometer (PACS; Poglitsch et al. 2010) at wavelengths of 100 and 160  $\mu\text{m}$ . SPIRE and PACS photometry for the H-ATLAS and HeLMS sources was taken from Zhang et al. (2018) and Nayyeri et al. (2016). Where possible, we have also used 850  $\mu\text{m}$  Submillimetre Common User Bolometer Array 2 (SCUBA-2) flux densities (14 arcsec resolution; Mackenzie et al. 2011) taken from Bakx et al. (2017), 880  $\mu\text{m}$  photometry taken from the Submillimetre Array (SMA) (0.6 arcsec

resolution) as described in Bussmann et al. (2013) and ALMA/ACA rest-frame 290 and 310  $\mu\text{m}$  photometry taken from Riechers et al. (2021). Finally, the ALMA band 4 (1940  $\mu\text{m}$ , 0.3 arcsec resolution) flux density for H-ATLAS J083051.0+01322 was taken from Yang et al. (2019b). We searched the *Herschel* Extragalactic Legacy Project (HELP; Shirley et al. 2021) data base for additional information, but were unable to find unambiguous matches to our sources.

The available lens and source redshifts for the seven systems modelled in this paper can be found in Table 2. The observed photometry can be found in Table 3.

### 3 METHODOLOGY

#### 3.1 The semi-linear inversion method in the uv-plane

The standard image plane approach of the semi-linear inversion method makes use of a pixelized source plane. For a given lens model, the image of each pixel is formed and the linear superposition of these images that best fits the data determines the source surface brightness distribution. Analogously to the image plane version, when working with interferometer visibility data, a model set of visibilities is formed for an image of each source pixel. The linear combination of these model visibilities determines the source surface brightness distribution for a particular lens model.

We used the source inversion method implemented within `PyAutoLens` (Nightingale et al. 2021), which is based on the operator approach described within Powell et al. (2020). An interferometer visibility data set  $\mathbf{d}$  is comprised of samples of complex visibilities. The surface brightness in the source plane is given by the vector  $\mathbf{s}$ , with each element corresponding to the surface brightness of a source plane pixel. The parametrized projected surface mass density of the lens model is given by the vector  $\boldsymbol{\eta}$  and the mapping of the source light  $\mathbf{s}$  to the image plane is described by the operator  $\mathbf{L}(\boldsymbol{\eta})$ . The sky brightness is therefore simply  $\mathbf{L}(\boldsymbol{\eta})\mathbf{s}$ . The response of an interferometer is encoded into the operator  $\mathbf{D}$ , which performs the Fourier transforms to convert the pixelized sky brightness distribution into a set of complex visibilities. The observed data  $\mathbf{d}$  can therefore be described by the combination of these effects:

$$\mathbf{d} = \mathbf{D}\mathbf{L}(\boldsymbol{\eta})\mathbf{s} + \mathbf{n}. \quad (1)$$

Assuming uncorrelated Gaussian noise  $\mathbf{n}$  in the observed visibility data, the noise covariance can be represented by the diagonal matrix  $\mathbf{C}^{-1}$ . The uncertainties on visibilities are often set to arbitrary values, or estimated from poorly understood antenna and receiver properties. This can lead to problems when accurate uncertainties are required, such as for performing visibility data lens modelling. Using a similar method to Dye et al. (2018) to determine the  $1\sigma$  uncertainties on the visibilities, we used the `CASA` task `statwt` to empirically measure

**Table 2.** The list of the seven lensing systems modelled in this work, along with their lens galaxy redshifts,  $z_1$ , and their background source redshifts  $z_s$ . Where appropriate, the redshift of both lensing galaxies have been provided, distinguished by the numbered subscript.

ID	Short name	Alternative name	$z_{1,1}$	$z_{1,2}$	$z_s$
H-ATLAS J083051.0+013225	G09v1.97	–	0.626 <sup>b</sup>	1.002 <sup>b</sup>	3.634 <sup>a</sup>
HeLMS J005159.4+062240	HELMS18	HeLMS-9	0.602 <sup>d</sup>	0.599 <sup>d</sup>	2.3934 <sup>e</sup>
HeLMS J234051.5-041938	HELMS5	HeLMS-62	–	N/A	3.5027 <sup>e</sup>
HeLMS J232439.5-043935	HELMS7	HeLMS-45	–	–	2.4726 <sup>e</sup>
HeLMS J233255.4-031134	HELMS2	HeLMS-44	0.426 <sup>c</sup>	N/A	2.6895 <sup>e</sup>
HeLMS J233255.6-053426	HELMS15	HeLMS-61	0.976 <sup>c</sup>	N/A	2.4022 <sup>e</sup>
HeLMS J235331.9+031718	HELMS40	–	0.821 <sup>c</sup>	N/A	2.0 – 3.7

*Notes.* The references from which the lens and source redshifts were obtained are as follows: <sup>a</sup>Bussmann et al. (2013); <sup>b</sup>Negrello et al. (2017); <sup>c</sup>Nayyeri et al. (2016); <sup>d</sup>Okido et al. (2020); and <sup>e</sup>Riechers et al. (2021). The range of redshifts given for HeLMS J235331.9+031718 is an assumption based on the range of source redshifts in this paper, since there is no available redshift measurement for this source. A dash indicates missing redshift information for a lens, whilst ‘N/A’ is used to indicate a second mass profile was not used in our modelling procedure. A list of short names is provided that may be used throughout this paper; these names are consistent with Nayyeri et al. (2016) and Bussmann et al. (2013). A list of alternate names that have been used to describe these sources (e.g. in Riechers et al. 2021) is also provided to emphasize that these are indeed the same sources.

**Table 3.** Observed (i.e. lensed) source flux densities in mJy. The passband central wavelength in  $\mu\text{m}$  is indicated by the subscripts. For both the H-ATLAS and HeLMS sources, the flux densities  $f_{100}$  to  $f_{500}$  are taken from Zhang et al. (2018) and Nayyeri et al. (2016). The flux densities  $f_{850}$ ,  $f_{873}$ ,  $f_{880}$ , and  $f_{1940}$  are taken from Bakx et al. (2017), this work, Bussmann et al. (2013) and Yang et al. (2019b), respectively. The flux densities  $f_{290}^{\text{rest}}$  and  $f_{310}^{\text{rest}}$  are rest-frame quantities and are taken from Riechers et al. (2021).

ID	$f_{100}$ (mJy)	$f_{160}$ (mJy)	$f_{250}$ (mJy)	$f_{350}$ (mJy)	$f_{500}$ (mJy)	$f_{850}$ (mJy)	$f_{873}$ (mJy)	$f_{880}$ (mJy)	$f_{1940}$ (mJy)	$f_{290}^{\text{rest}}$ (mJy)	$f_{310}^{\text{rest}}$ (mJy)
G09v1.97	$53 \pm 3$	$198 \pm 10$	$260 \pm 7$	$321 \pm 8$	$269 \pm 9$	$121 \pm 9$	$92 \pm 9$	$86 \pm 4$	$8.8 \pm 0.5$	–	–
HELMS18	$31 \pm 3$	$91 \pm 15$	$166 \pm 6$	$195 \pm 6$	$135 \pm 7$	–	$41 \pm 4$	–	–	$29.6 \pm 1.7$	–
HELMS5	$7 \pm 3$	$68 \pm 7$	$151 \pm 6$	$209 \pm 6$	$205 \pm 8$	–	$94 \pm 9$	–	–	$32.15 \pm 0.43$	$21.79 \pm 0.90$
HELMS7	$33 \pm 4$	$129 \pm 7$	$214 \pm 7$	$218 \pm 7$	$172 \pm 9$	–	$36 \pm 4$	–	–	$22.3 \pm 1.2$	–
HELMS2	$25 \pm 4$	$146 \pm 14$	$271 \pm 6$	$336 \pm 6$	$263 \pm 8$	–	$75 \pm 8$	–	–	$39.3 \pm 1.1$	–
HELMS15	$14 \pm 3$	$44 \pm 8$	$148 \pm 6$	$187 \pm 6$	$147 \pm 9$	–	$48 \pm 5$	–	–	$32.89 \pm 0.78$	–
HELMS40	–	–	$102 \pm 6$	$123 \pm 7$	$111 \pm 7$	–	$26 \pm 3$	–	–	–	–

the visibility scatter computed over all baselines, ensuring reasonable uncertainties on all visibilities.

Combining equation (1) with the set of model visibilities  $\mathbf{DL}(\eta)s$  allows us to write the  $\chi^2$  statistic as

$$\chi^2 = (\mathbf{DL}s - \mathbf{d})^T \mathbf{C}^{-1} (\mathbf{DL}s - \mathbf{d}). \quad (2)$$

With the addition of a prior on the source denoted by the operator  $\mathbf{R}$  and with the regularization strength given by  $\lambda_s$ , Powell et al. (2020) show that we can write the regularized least-squares equation as

$$[(\mathbf{DL})^T \mathbf{C}^{-1} \mathbf{DL} + \lambda_s \mathbf{R}^T \mathbf{R}] s_{\text{MP}} = (\mathbf{DL})^T \mathbf{C}^{-1} \mathbf{d}, \quad (3)$$

where the maximum a posteriori source inversion matrix (i.e. the solution matrix for  $s_{\text{MP}}$ ) is given by the quantity in square brackets in equation (3). This linear system of equations is in principle straightforward to solve, but becomes extremely memory intensive for large numbers of visibilities and/or large numbers of source plane pixels. For this reason, a direct Fourier transform is replaced by a non-uniform fast Fourier transform, constructed out of a series of operators. This substitution results in a modified version of equation (3), where the solution for  $s_{\text{MP}}$  is given by a series of operators evaluated by use of an iterative linear solver (see Powell et al. 2020; Nightingale et al. 2021 for more details on this methodology and the specific implementation used here).

To find the optimal lens model parameters with PyAutoLens, we used the nested sampling algorithm *dynesty* (Speagle 2020) to maximize the Bayesian evidence as derived within Suyu et al. (2006). We adopted a gradient regularization scheme, analogous to that which

is described in Warren & Dye (2003), with a constant weight for the source plane due to its simplicity and to not add more computational costs to an already expensive procedure. Other techniques, such as those that use multiple regularization weights adapted to the surface brightness in the source plane require introducing more free parameters to be fitted, and thus increase the complexity of the problem. When dealing with data sets containing many visibilities, such a process takes 2–3 d running the analysis on a 2020 model Macbook Air with PyAutoLens v2021.10.14.1 and PYTHON v3.9.6. We first reconstructed the background source using a source plane pixelization adapted to the lens magnification. This magnification-based fit was then used to initialise a new search of parameter space with a source plane that adapted to the brightness of the reconstructed source (Nightingale & Dye 2015; Nightingale, Dye & Massey 2018). The mass model parameters, along with the source plane parameters (regularization, number of source plane pixels), were fully optimized throughout the lens modelling procedure.

### 3.2 Lens model

We have used the elliptical power-law density profile, which is a generalized form of the singular isothermal ellipsoid that is commonly used to fit strong lens profiles (Keeton 2001). When it improves the Bayesian evidence, an external shear component is included to compensate for the influence of line of sight galaxies that may be outside our field of view. Where indicated by additional

imaging or unusual image configurations, two elliptical power-law profiles have been used to model the group-scale lenses present in the sample. We find that in all cases this is sufficient to provide acceptable fits to the data and, through the use of optical/near-infrared imaging, we see no indication of more than two lenses being required to produce an accurate model. The surface mass density,  $\kappa$ , of this profile is given by

$$\kappa(R) = \frac{3 - \alpha}{1 + q} \left( \frac{\theta_E}{R} \right)^{\alpha-1}, \quad (4)$$

where  $\theta_E$  is the model Einstein radius in arc seconds,  $\alpha$  is the power-law index, and  $R$  is the elliptical radius defined as  $R = \sqrt{x^2 + y^2/q^2}$ , where  $q$  is the axial ratio (Suyu 2012). The lens orientation  $\phi$  is measured as the angle counterclockwise from the east axis to the semimajor axis of the elliptical lens profile. The centre of the lens profile is given by the coordinates in the image-plane ( $x_c$ ,  $y_c$ ). The external shear field is parameterised by a shear strength  $\gamma$  and shear direction  $\phi_\gamma$ , measured counterclockwise from east. The shear direction is defined to be perpendicular to the direction of the resulting image stretch. For single lens systems, there are six lens model parameters (eight when including external shear) and 12 lens model parameters (14 when including external shear) in the case of group-scale lenses.

## 4 RESULTS

Fig. 1 shows the model image, residual image and source reconstruction for each of the seven lenses modelled in this work. The lens model parameters from our fitting procedure are given in Table 4.

Different interferometer configurations probe distinct scales and reach varying surface brightness limits. Fig. 2 shows how, for each system, the inferred magnification is sensitive to this effect. By working down a list of a subset of source-plane pixels ordered by their flux density (and chosen to have a surface brightness above a certain threshold), the lensed image and average magnification of these pixels was computed. The source flux density fraction tells us how much of the total flux density is contained within the subset of source-plane pixels as we move down the list. Likewise, the image flux density fraction tells us how much of the total image flux density is contributed by the lensed image of our subset of source-plane pixels. This process was repeated 100 times using a randomized source plane pixelization for each, to produce an averaged magnification profile.

### 4.1 Intrinsic source properties

For each lens system, we have determined the intrinsic properties of the background source. To achieve this, we have demagnified the submm photometry (see Table 3) by the total source magnification factors given in Table 5, taking into account the uncertainties on our magnification values. With the source redshifts given in Table 2, we fitted the rest-frame photometry with two spectral energy distributions (SEDs). First, a single temperature, optically thick SED was fitted, of the form:

$$S_\nu \propto [1 - \exp(-(\nu/\nu_0)^\beta)] B(\nu, T_d), \quad (5)$$

where  $S_\nu$  is the flux density at frequency  $\nu$ ,  $\nu_0$  is the frequency at which the optical depth is equal to unity,  $\beta$  is the dust emissivity index,  $T_d$  is the dust temperature, and  $B(\nu, T_d)$  denotes the Planck function. Second, a dual temperature, optically thin SED was fitted, of the form:

$$S_\nu = \nu^\beta [N_c B(\nu, T_c) + N_w B(\nu, T_w)], \quad (6)$$

where  $N$  is the weighting of the cold and warm components (denoted with subscripts) and  $T$  is the dust temperature of the two components (denoted by the subscripts). This approach of using both a single-temperature and dual-temperature SED model allows for the computation of a reasonable upper and lower bound on the range of possible dust masses, which were determined using the method described in Dunne et al. (2011). In this work, we have used the 873  $\mu\text{m}$  ALMA flux density and computed the dust mass absorption coefficient by extrapolating the 850  $\mu\text{m}$  value of  $\kappa_{850} = 0.077 \text{ m}^2 \text{ kg}^{-1}$  (James et al. 2002 – see Dunne et al. 2000 for more details). The uncertainties in the dust mass absorption coefficient are known to be large, but a relative comparison between dust masses computed with this value is still valuable. The same value of  $\kappa_{873}$  was used for all of our galaxies, which assumes that the physical properties of the dust, such as grain size and density, are constant for our sample of galaxies. The scaling relations from Hughes et al. (2017) were used to calculate the  $\text{H}_2$  gas mass.

During the fitting of the optically thin SED, the temperature and normalization of both dust components were allowed to vary. In the case of the optically thick SED, the temperature, normalization, and opacity at 100  $\mu\text{m}$ ,  $\tau_{100}$ , were varied during the fit. Throughout, the emissivity index,  $\beta$ , was fixed to 2.0 (see Smith et al. 2013). The fitted SEDs and the demagnified source photometry can be seen in Fig. 3. The best-fitting parameters for these SEDs can be found in Table 5, along with the demagnified luminosity of the sources, computed by integrating the optically thin SED from 3 to 1100  $\mu\text{m}$ . The uncertainty on the luminosity includes a propagation of the error from the magnification factors, as well as the uncertainties on the fitted parameters of the SED, included via a Monte Carlo approach. The quoted uncertainties in Table 5 are the  $1 - \sigma$  bounds given by Dynesty (Speagle 2020) and the posterior distributions do not exhibit significant tails. Finally, the SFRs of the sources are given, computed using the conversion from luminosity

$$\log(\text{SFR}) = \log(L_{\text{IR}}) - 43.41 \quad (7)$$

given by Kennicutt & Evans (2012), who employ the initial mass function (IMF) of Kroupa (2001). This conversion assumes that all the infrared emission originates from star-forming regions, which may result in biased SFR values if an active galactic nucleus (AGN) is significantly contributing to the luminosity of the galaxy.

### 4.2 Object notes

#### 4.2.1 H-ATLAS J083051.0+013225

This lens system has an almost complete  $\sim 1.5$  arcsec Einstein ring with three major image components, along with a fainter central image. The central image is due to the rare line of sight configuration of the dual deflectors. Keck Adaptive Optics  $K_s$  band imaging of this lensing system (see Calanog et al. 2014) shows two galaxies, but the lensing features are ambiguous due to the low signal-to-noise ratio. Upon superimposing the lensed emission from the background source as detected in ALMA data, it is clear that both of these galaxies are interior to the Einstein ring (see Yang et al. 2019b). Long slit spectroscopy, presented in Bussmann et al. (2013), provides evidence that these two galaxies are at different redshifts (0.626 and 1.002, respectively). Bussmann et al. (2013) present the modelling of SMA data for this system, fitting two SIE models for the foreground deflectors and a Sérsic model for the background source. They infer a magnification factor  $\mu = 6.9 \pm 0.6$ , which is in agreement with the magnification we find with our best-fitting model of  $\mu = 6.7 \pm 0.5$ . Yang et al. (2019b) present ALMA band 4 data, along with the

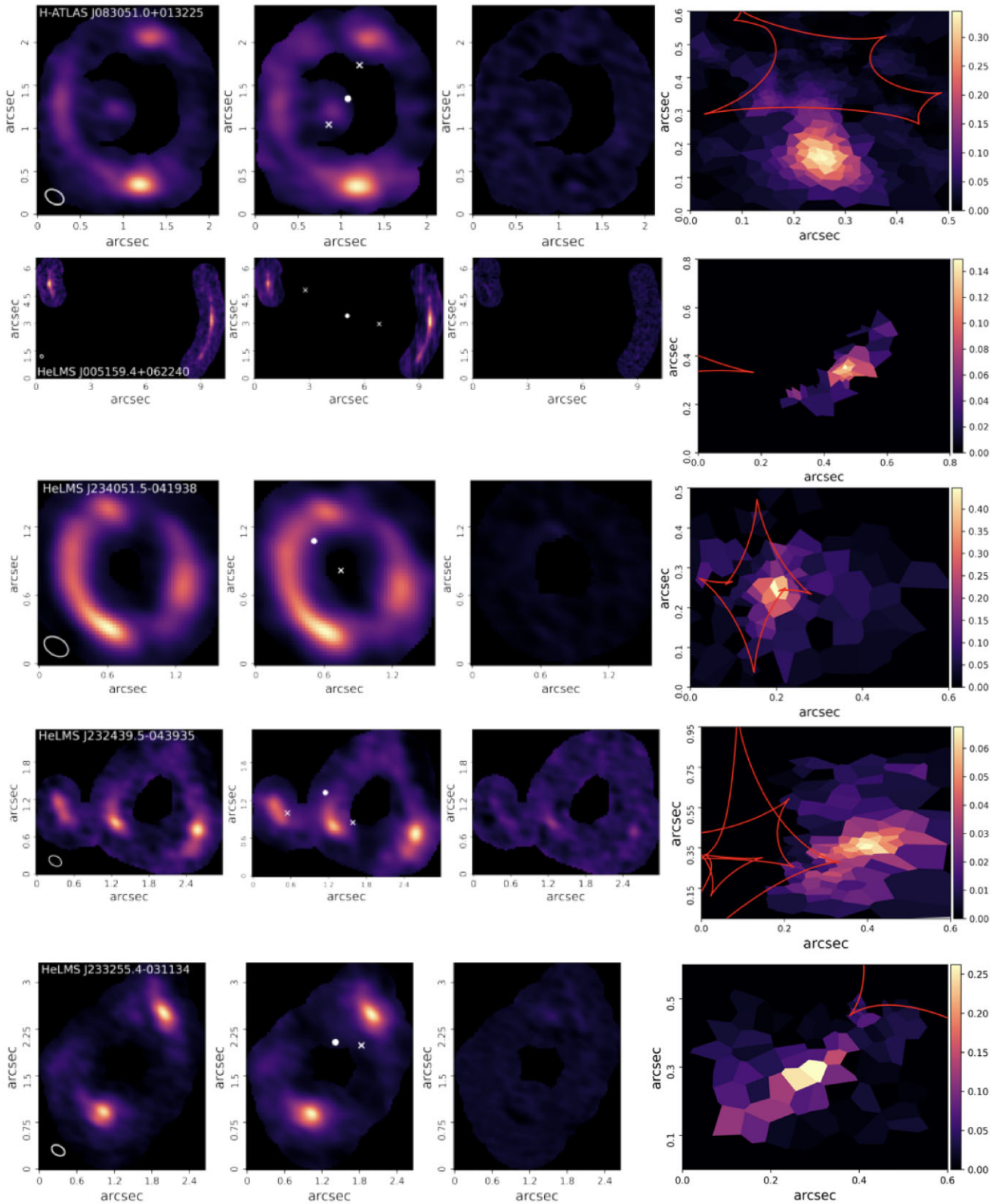


**Figure 1.** Lens reconstructions for each system. The left column shows the cleaned ALMA image. The middle left column shows the lensed image of our reconstructed source, i.e. the model image with the lens centroid(s) and centre of the source plane indicated by white crosses and white circles, respectively. The middle right column shows the residual image for our model, i.e. the image of the observed visibilities minus the image of the model visibilities. The right column shows the reconstructed source. The colour bar indicates the  $873 \mu\text{m}$  surface brightness in  $\text{Jy arcsec}^{-2}$  for each of the panels related to a particular source and all residuals are  $<3\sigma$ . The caustics are shown in red. North is up and east is left. The beam is shown as a white ellipse in the bottom left corner of the cleaned ALMA images.

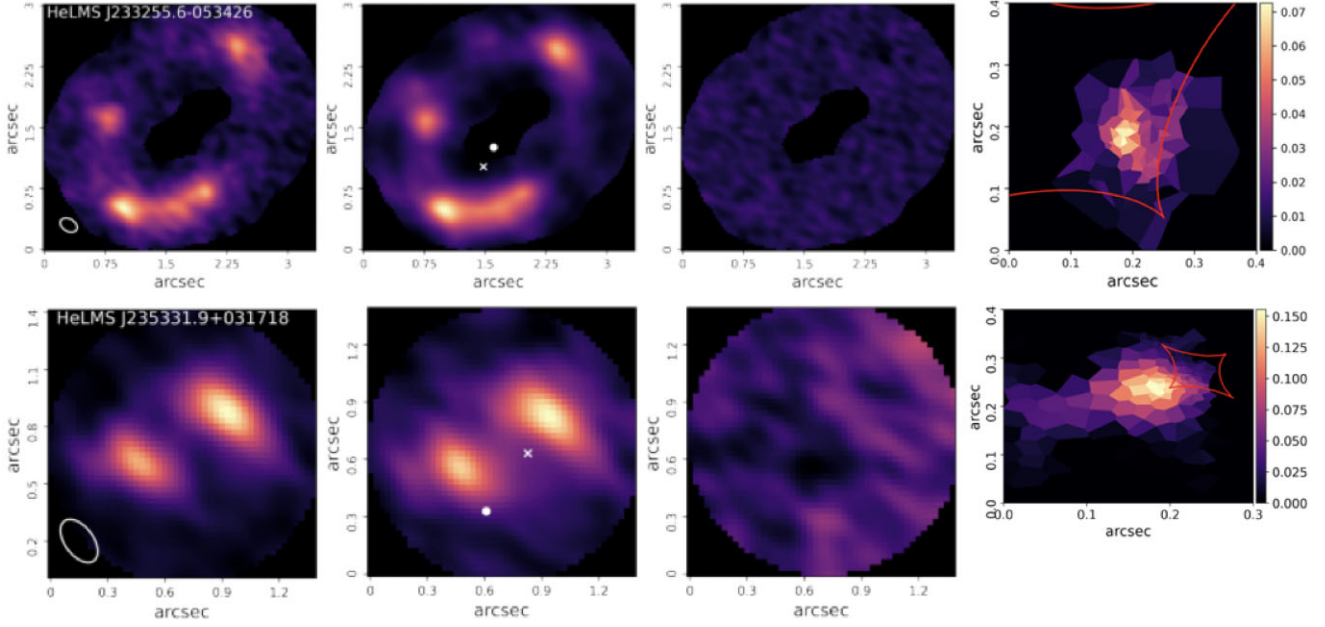


Figure 1 – continued

**Table 4.** Lens model parameters. The columns are the Einstein radius,  $\theta_E$ , coordinates  $(x_c, y_c)$  of the centroid of the mass profile with respect to the phase-tracking centre of the observations ( $x_c$  and  $y_c$  correspond to west and north respectively), the lens profile orientation measured as the angle counterclockwise from east to the semi major axis,  $\phi$ , the lens profile axial ratio,  $q$ , the density slope of the power-law,  $\alpha$ , the magnitude of the external shear field,  $\gamma$ , and the external shear field direction,  $\phi_\gamma$ , measured counterclockwise from east.

ID	$\theta_E$ (arcsec)	$(x_c, y_c)$ (arcsec)	$\phi$ (deg)	$q$	$\alpha$	$\gamma$	$\phi_\gamma$ (deg)
G09v1.97 (lens 1)	$0.43 \pm 0.01$	$(-1.87 \pm 0.01, -0.78 \pm 0.01)$	$7 \pm 1$	$0.51 \pm 0.01$	$2.18 \pm 0.02$	–	–
G09v1.97 (lens 2)	$0.54 \pm 0.01$	$(-1.51 \pm 0.01, -0.08 \pm 0.01)$	$9 \pm 2$	$0.90 \pm 0.01$	$2.03 \pm 0.08$	–	–
HELMS18 (lens 1)	$3.80 \pm 0.02$	$(-4.67 \pm 0.01, 4.02 \pm 0.01)$	$156 \pm 2$	$0.37 \pm 0.05$	$2.05 \pm 0.03$	$0.17 \pm 0.02$	$102 \pm 3$
HELMS18 (lens 2)	$1.46 \pm 0.02$	$(-0.63 \pm 0.01, 2.18 \pm 0.01)$	$109 \pm 5$	$0.66 \pm 0.06$	$1.93 \pm 0.02$	–	–
HELMS5	$0.75 \pm 0.01$	$(-0.78 \pm 0.01, -1.88 \pm 0.01)$	$97 \pm 1$	$0.27 \pm 0.01$	$2.37 \pm 0.01$	$0.17 \pm 0.01$	$103 \pm 1$
HELMS7 (lens 1)	$0.54 \pm 0.01$	$(1.91 \pm 0.02, 1.09 \pm 0.02)$	$23 \pm 1$	$0.79 \pm 0.02$	$2.08 \pm 0.06$	$0.13 \pm 0.01$	$165 \pm 2$
HELMS7 (lens 2)	$0.40 \pm 0.01$	$(0.88 \pm 0.01, 1.24 \pm 0.01)$	$84 \pm 2$	$0.27 \pm 0.02$	$1.84 \pm 0.03$	–	–
HELMS2	$1.01 \pm 0.01$	$(-0.06 \pm 0.01, -1.52 \pm 0.02)$	$118 \pm 2$	$0.44 \pm 0.02$	$1.89 \pm 0.01$	$0.18 \pm 0.01$	$112 \pm 1$
HELMS15	$1.05 \pm 0.01$	$(2.43 \pm 0.01, 0.18 \pm 0.01)$	$150 \pm 1$	$0.56 \pm 0.01$	$1.99 \pm 0.03$	$0.12 \pm 0.01$	$48 \pm 1$
HELMS40	$0.21 \pm 0.01$	$(1.81 \pm 0.01, 1.32 \pm 0.01)$	$151 \pm 4$	$0.49 \pm 0.05$	$1.64 \pm 0.04$	$0.19 \pm 0.02$	$170 \pm 5$

band 7 data presented in this paper, and find a significantly higher magnification factor of  $\mu = 10.5^{+0.5}_{-0.6}$ , using a double SIE lens model and a dual disc model for the background source.

The peak of the SED is bounded by the SPIRE photometry and shows some evidence of a significant warm dust component. This is reflected in the fact that the dual-temperature SED is the statistically preferred model.

The SFR of this lensed source is extremely high at  $3700 \pm 500 M_\odot \text{ yr}^{-1}$ , in reasonable agreement with the value reported by Zhang et al. (2018), who used the magnification factor from Bussmann et al. (2013) to determine the SFR. This compares to the lower values of SFR inferred by Yang et al. (2019b) who find  $600 \pm 300 M_\odot \text{ yr}^{-1}$  and  $900 \pm 400 M_\odot \text{ yr}^{-1}$  for each of the components in their source model. Our value of SFR is reduced to  $2400 M_\odot \text{ yr}^{-1}$  when using the magnification factor of 10.5 found by Yang et al. (2019b). A possible explanation for the large discrepancy in SFR is differential magnification of the source. Yang et al. (2019b) find evidence of differential magnification for the compact and extended components of their source model, which they have taken

into account in their SED modelling. In addition to this, whilst the lens model that we find is similar to that of Yang et al. (2019b), we have allowed the power-law slope to vary rather than using SIE profiles. The higher values ( $>2$ ) of slope that we find will tend to decrease the overall magnification of the source plane.

Our reconstructed source for this system shows significant disturbance, with a main component oriented north–south and a fainter component oriented east–west.

#### 4.2.2 HeLMS J005159.4+062240

This system is a group-scale lens with a doubly-imaged background source. Optical imaging from the Sloan Digital Sky Survey Data Release 14 (Abolfathi et al. 2018) reveals two lensing galaxies within the lensed arcs. Tergolina (2020) investigated these objects, finding that one was a red and passive early-type galaxy (ETG;  $z = 0.60246 \pm 0.00004$ ), whilst the other is the host of a quasar ( $z = 0.59945 \pm 0.00009$ ; Okido et al. 2020). We were able to find a lens model constructed from two elliptical power-law density profiles and

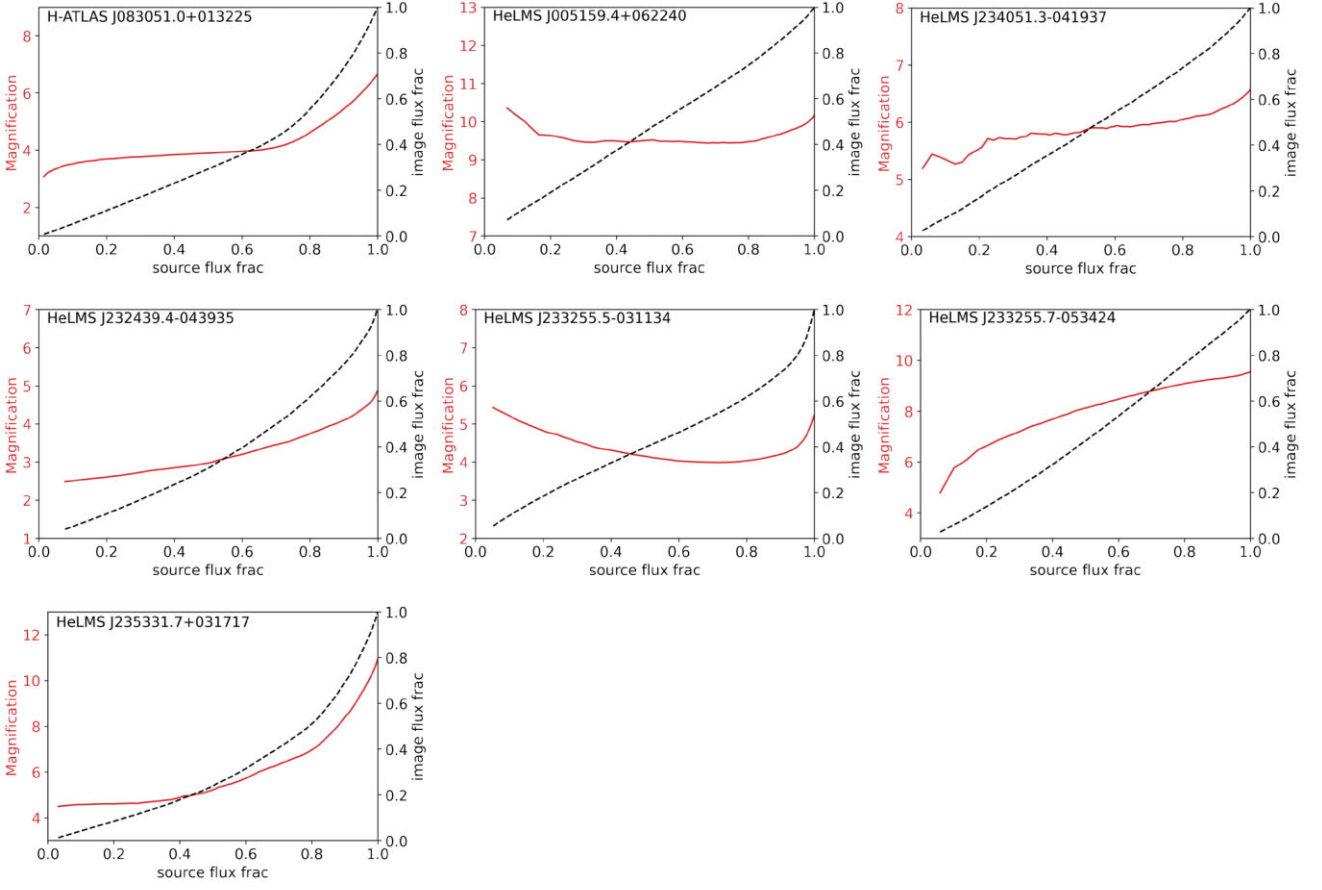


**Figure 2.** The magnification profile for each of the reconstructed background sources. Each plot shows how the total magnification (solid red line) and image flux density fraction (dashed black line) varies as a function of the source flux density fraction above a surface brightness threshold (more details given in the main text). The magnification profiles represent the average of 100 realizations of the source plane pixelization for the best-fitting lens model. The plot demonstrates how the inferred magnification can vary with different interferometer configurations.

**Table 5.** Intrinsic source properties. The columns are total magnification,  $\mu_{\text{tot}}$ , dust mass computed from the single temperature optically thick SED,  $M_{\text{d}}^{\text{thick}}$ , dust mass assuming a dual temperature optically thin SED,  $M_{\text{d}}^{\text{thin}}$ , temperature of the optically thick SED,  $T^{\text{thick}}$ , temperatures of the optically thin SED,  $T^{\text{thin}}$ , the optical depth at  $100 \mu\text{m}$  for the optically thick SED,  $\tau_{100}$ , the demagnified luminosity (computed as the integral of the optically thin SED from  $3$  to  $1100 \mu\text{m}$ ),  $L_{\text{IR}}$ , the  $\text{H}_2$  gas mass computed using the scaling relation of Hughes et al. (2017),  $M_{\text{gas}}$ , and the SFR scaled from  $L_{\text{IR}}$  using the procedure given by Kennicutt & Evans (2012) with a Kroupa IMF. The two dust masses given in this table are intended as reasonable upper and lower bounds, as discussed in Section 4. The source HeLMS J235331.9+031718 appears twice, displaying the intrinsic source properties for the upper and lower value of source redshift being considered (indicated in the ID column).

ID	$\mu_{\text{tot}}$	$M_{\text{d}}^{\text{thick}}$ $\log(M_{\text{d}}/M_{\odot})$	$M_{\text{d}}^{\text{thin}}$ $\log(M_{\text{d}}/M_{\odot})$	$T^{\text{thick}}$ (K)	$T^{\text{thin}}$ (K)	$\tau_{100}$	$L_{\text{IR}}$ $\log(L_{\text{IR}}/L_{\odot})$	$M_{\text{gas}}$ $\log(M_{\text{gas}}/M_{\odot})$	SFR ( $M_{\odot} \text{ yr}^{-1}$ )
G09v1.97	$6.7 \pm 0.5$	8.5	9.2	$86 \pm 2$	$31_{-2}^{+1}/69_{-2}^{+3}$	$6.5 \pm 1.0$	$13.4 \pm 0.1$	$11.3 \pm 0.5$	$3700 \pm 500$
HELMS18	$10.2 \pm 0.5$	8.2	8.9	$63 \pm 2$	$27 \pm 1/56_{-4}^{+5}$	$6.7 \pm 0.9$	$12.6 \pm 0.1$	$11.0 \pm 0.6$	$600 \pm 100$
HELMS5	$6.7 \pm 0.5$	8.3	9.1	$62 \pm 2$	$28 \pm 1/53_{-3}^{+4}$	$5.3 \pm 0.8$	$13.1 \pm 0.1$	$11.4 \pm 0.6$	$1900 \pm 300$
HELMS7	$4.9 \pm 0.5$	8.5	9.1	$63 \pm 2$	$31 \pm 2/54_{-7}^{+6}$	$3.6 \pm 0.6$	$13.0 \pm 0.1$	$11.2 \pm 0.7$	$1500 \pm 300$
HELMS2	$5.5 \pm 0.5$	8.5	9.1	$59 \pm 2$	$29 \pm 1/52_{-2}^{+4}$	$4.2 \pm 0.7$	$13.1 \pm 0.1$	$11.5 \pm 0.5$	$1900 \pm 300$
HELMS15	$9.2 \pm 0.5$	8.5	9.0	$46_{-3}^{+2}$	$27 \pm 1/54_{-7}^{+9}$	$4.1 \pm 0.7$	$12.5 \pm 0.1$	$11.2 \pm 0.7$	$500 \pm 100$
HELMS40 ( $z = 2.0$ )	$8.7 \pm 0.5$	8.7	9.0	$32_{-2}^{+5}$	$25_{-3}^{+2}/55_{-22}^{+33}$	$1.5 \pm 0.7$	$12.2_{-0.1}^{+0.4}$	$11.1 \pm 0.8$	$230_{-50}^{+300}$
HELMS40 ( $z = 3.7$ )	$8.7 \pm 0.5$	8.2	8.5	$43_{-2}^{+3}$	$39_{-2}^{+1}/64_{-27}^{+24}$	$0.3 \pm 0.1$	$12.7_{-0.1}^{+0.2}$	$10.9 \pm 0.8$	$800_{-100}^{+400}$

an external shear field that reconstructs the background source as a single component. Our reconstructed source appears elongated with a disturbed morphology.

With a magnification factor of  $\mu = 10.2 \pm 0.5$ , this system has the highest total magnification in our sample. Our measurement

of the intrinsic source luminosity,  $\log(L_{\text{IR}}/L_{\odot}) = 12.6 \pm 0.1$ , is in reasonable agreement with the far-infrared (far-IR) luminosity given in Nayyeri et al. (2016), once the lens magnification has been taken into account. It is unlikely that the quasar, hosted in one of the lens galaxies, is contributing to the infrared luminosity, as it is



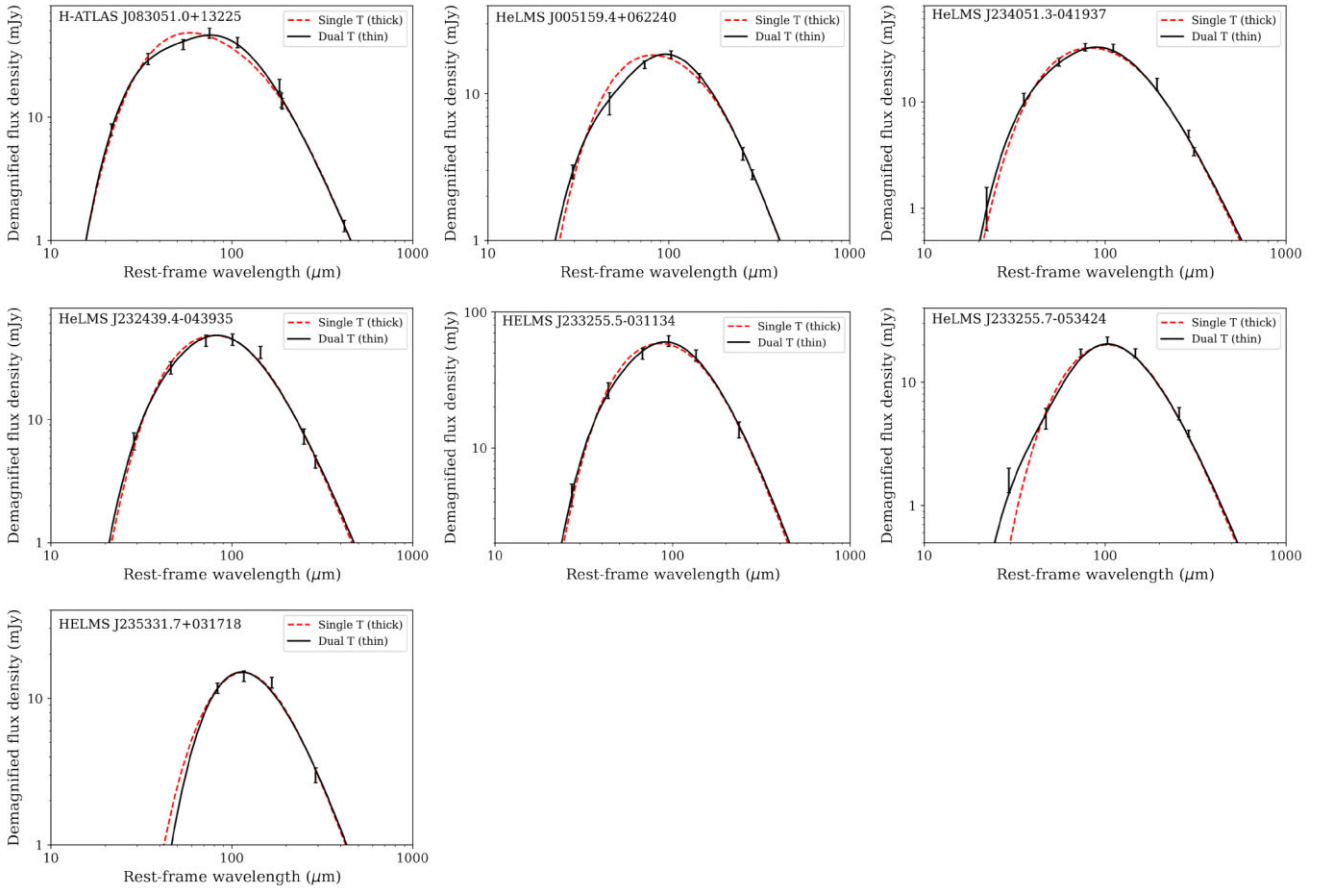


**Figure 3.** SEDs of the lensed background sources. The two-temperature optically thin fit (solid black line) and the single-temperature optically thick fit (dashed red line) are shown in each subplot. The measured photometry and uncertainties, shown as the error bars in the plots, have been demagnified by the appropriate lensing magnifications  $\mu$ , given in Table 5. The SED for HeLMS J235331.7+031718 is shown at a redshift of  $z = 2$ .

not detected at the lens centroid in our ALMA data. The peak of the SED is bounded by the SPIRE photometry, and the PACS flux densities indicate the presence of a warm dust component. As such, the two temperature SED provides a better fit to the data, and is the statistically preferred model of the two. With an SFR of  $\sim 590 \pm 50 M_{\odot} \text{ yr}^{-1}$  and a dust mass range of  $10^{8.2} - 10^{8.9} M_{\odot}$ , this source’s SFR to dust mass ratio is typical of high-redshift SMGs and low redshift ULIRGs according to the empirical relations in Rowlands et al. (2014).

#### 4.2.3 HeLMS J234051.5-041938

This system displays a nearly-complete  $\sim 0.75$  arcsec Einstein ring with three image components. A singular power law with external shear provides a good fit to the data, with the power-law index preferring relatively high values of around 2.3. The source has evidence of a disturbed morphology, displaying extended faint emission to the west and east.

The peak of the source SED is constrained by our ALMA and SPIRE photometry. The PACS flux densities do not indicate the presence of a significant warm dust component, with both the single and double temperature SEDs providing excellent fits to the data. The dual-temperature SED is the statistically preferred model.

This source’s intrinsic luminosity of  $\log(L_{\text{IR}}/L_{\odot}) = 13.1 \pm 0.1$  agrees well with the luminosity calculated by Nayyeri et al. (2016). An SFR of  $\sim 1900 \pm 300 M_{\odot} \text{ yr}^{-1}$  and a dust mass range of  $10^{8.3} -$

$10^{9.1} M_{\odot}$  places this source above the typical dust mass to SFR ratio for high-redshift SMGs and local ULIRGs.

#### 4.2.4 HeLMS J232439.5-043935

This system exhibits an unusual image configuration with three distinct image components, the two westernmost of which show faint extended features, whilst the eastern component is more compact. Two power-law density profiles with an external shear field provide an excellent fit to the data, reconstructing a source with faint extended emission to the north.

The peak in flux density for this source occurs close to the 250  $\mu\text{m}$  SPIRE measurement, with the constraints coming from the PACS measurements. The SED does not show clear evidence of a significant second temperature component, with both SED models providing good fits to the measured flux densities. The single temperature model is statistically preferred.

With an intrinsic luminosity of  $\log(L_{\text{IR}}/L_{\odot}) = 13.0 \pm 0.1$ , our estimate is consistent within our uncertainties of the value given by Nayyeri et al. (2016). An SFR of  $\sim 1500 \pm 300 M_{\odot} \text{ yr}^{-1}$  and a dust mass range of  $10^{8.5} - 10^{9.1} M_{\odot}$  means that this source has a higher than typical ratio of SFR to dust mass for high-redshift SMGs and local ULIRGs.

#### 4.2.5 HeLMS J233255.4-031134

This is a doubly-imaged source with some faint extended emission emanating from the southern image; it is well fit by a single power-

law density profile and an external shear field. The reconstructed source is relatively compact and featureless.

The peak of the SED is constrained by the SPIRE photometry, with the PACS flux densities not showing any major warm dust component. The SED is well described by an optically thick model, but the optically thin model provides a marginally better fit.

The intrinsic source luminosity we have obtained of  $\log(L_{\text{IR}}/L_{\odot}) = 13.1 \pm 0.1$  is in agreement with Nayyeri et al. (2016). The SFR of  $\sim 2000 \pm 300 M_{\odot} \text{ yr}^{-1}$  for this source agrees with the value quoted by Zhang et al. (2018) within our stated uncertainties. A dust mass range of  $10^{8.5} - 10^{9.1} M_{\odot}$  means that this galaxy also lies above the mean SFR to dust mass ratio, as given by Rowlands et al. (2014).

#### 4.2.6 HeLMS J233255.6-053426

This quadruple image system is well described by a power-law density profile embedded in an external shear field. The source exhibits a relatively featureless, compact morphology. The peak of the source SED is well constrained by the ALMA and SPIRE photometry. The PACS photometry indicates the presence of a warmer dust component, as shown by the relatively high  $100 \mu\text{m}$  PACS flux density measurement, and the significantly better fit of the two temperature SED. The dual-temperature SED is the statistically preferred model. Our measurement of the intrinsic source luminosity,  $\log(L_{\text{IR}}/L_{\odot}) = 12.5 \pm 0.1$ , is in agreement with the far-IR luminosity given in Nayyeri et al. (2016) using our magnification factor of 9.2 to demagnify the quoted value. With an SFR of  $\sim 500 \pm 50 M_{\odot} \text{ yr}^{-1}$  and a dust mass range of  $10^{8.5} - 10^{9.0} M_{\odot}$ , this source's SFR to dust mass ratio is consistent with typical high-redshift SMGs and low redshift ULIRGs as determined by the empirical relations given in Rowlands et al. (2014).

#### 4.2.7 HeLMS J235331.9+031718

This double image system has an extremely small image separation, with an Einstein radius of  $\sim 0.1$  arcsec. This system is described by a single power-law density profile and an external shear field. The inferred slope of the power-law density profile is relatively low at  $\alpha = 1.64 \pm 0.04$ , contributing to the high magnification of this source, which also lies near a lensing caustic cusp. The source itself appears to be mostly compact, with an extended feature to the southeast, which is readily visible in the observed lensed image.

There is no redshift measurement for this source, and so we have opted to use the range of redshifts ( $z \sim 2-3.7$ ) present in our sample to calculate redshift dependent quantities. There are also no PACS flux density measurements for this source, and so we rely on the SPIRE and ALMA measurements to constrain the SED. The peak of the SED appears to lie within the SPIRE wavelengths, and fitting the optically thick SED for the range of redshifts considered gives a temperature range of 37–59 K. Without the PACS measurements and with the extra free parameters of the optically thin SED, it is not possible to meaningfully infer the presence of a warmer dust component. This is reflected in the very large uncertainties on  $T_w$ , as shown in Table 5.

## 5 DISCUSSION

Combining our sample with that of Dye et al. (2018), who carried out a similar analysis on a set of 6 strongly lensed submm galaxies observed as part of the same ALMA programme, we can start to make

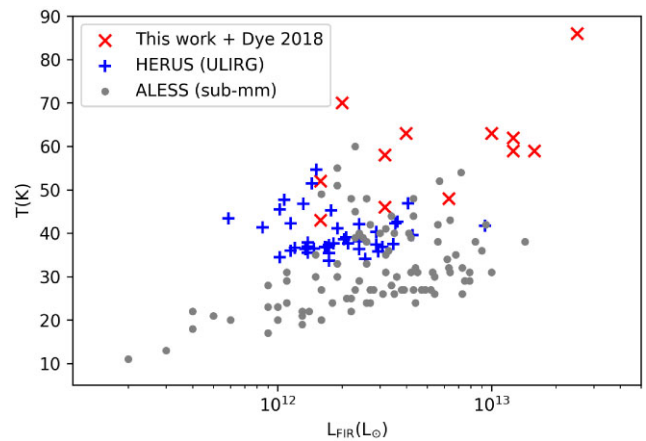


**Figure 4.** Temperature distribution as a function of far-IR luminosity. The red crosses show the luminosities taken from this work (excluding HeLMS J235331.9+031718), and Dye et al. (2018). The spectroscopic redshift range of this combined dataset is approximately  $z \sim 1-4$ . The blue pluses show the data taken from the HERUS Survey (Clements et al. 2017), with a spectroscopic redshift range of approximately  $z \sim 0.02-0.26$ . The grey dots come from the ALESS survey (Swinbank et al. 2013), with a photometric redshift range of  $z \sim 0.5-6.5$ .

more significant comparisons between our results and those found by other surveys. The HERschel ULIRG Survey (HERUS; Farrah et al. 2013) is a sample of 43 local ULIRGs, selected at  $60 \mu\text{m}$  by the Infrared Astronomical Satellite. This sample has been chosen as a characteristic sample of ULIRGs to compare against our sample of high-redshift SMGs, due to the similarity in available photometry constraining the SED (Clements et al. 2017). Comparisons to such a sample are useful in light of the often proposed evolutionary connection between SMGs and ULIRGs. However, it is important to note that the effective dust temperatures of the HERUS sample are derived from a modified blackbody SED of the form  $S_{\nu} \propto \nu^{\beta} B(\nu, T_d)$ , where the dust emissivity index is allowed to vary during the fit. The ULIRGs in the HERUS sample have a median dust emissivity index of  $\beta \sim 1.7$ , whereas we fixed the value of  $\beta = 2$  during our SED fitting procedure. The ALMA LESS survey is a set of cycle 0 and cycle 1 ALMA observations of the submm sources detected in the LABOCA ECDFS Submm Survey (LESS). The 126 ALMA LESS sources have a photometric redshift range of  $z \sim 1-6$ , and have been chosen as a typical sample of high redshift SMGs to compare against our own due to the similarity in available photometry constraining the SED. The characteristic dust temperatures of the ALMA LESS sources are once again derived from fitting a modified blackbody SED to the available photometry. Again, a significant difference in the methodology used is that the dust emissivity index was allowed to vary between 1 and 2.5 during the fitting procedure, whereas we have fixed its value to  $\beta = 2$ . Furthermore, the characteristic dust temperature is closely related to the wavelength of the peak of the SED, which for the case of the ALESS sample, is only determined via photometric redshifts. Comparing the relationship between the far-IR luminosity and the effective dust temperature (see Fig. 4) from the optically thick model between our sample, the ULIRG population from HERUS and the submm sources in ALESS, we can see that our sources tend to possess both more extreme luminosities and higher dust temperatures. The median luminosity of the ALESS sample is  $L_{\text{IR}} = (3.0 \pm 0.3) \times 10^{12} L_{\odot}$ , compared with the median luminosity of the HERUS sample of  $L_{\text{IR}} = (1.7 \pm 0.3) \times 10^{12} L_{\odot}$ , and finally, that of our sample:  $L_{\text{IR}} = (5.1 \pm 2.5) \times 10^{12} L_{\odot}$ . Given our small

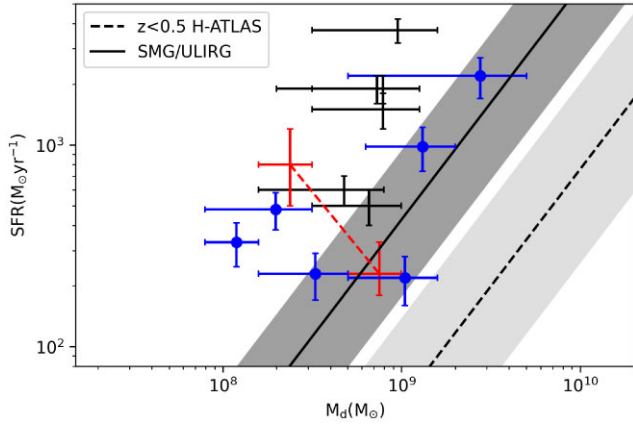


**Figure 5.** SFR, computed with the method of Kennicutt & Evans (2012), plotted against dust masses for our seven lensed sources (black pluses), with the six sources from Dye et al. (2018) shown as blue pluses with a central circle. The horizontal error bars represent the range of dust masses for each source encompassed by  $M_d^{\text{thick}}$  and  $M_d^{\text{thin}}$ , whilst the vertical error bars represent the uncertainty in SFR, plotted at the mid-point of the dust mass range. Shown in red are the values for the two extremes of redshift for HeLMS J235331.9+031718. Also shown are the empirical relations between  $M_d$  and SFR determined by Rowlands et al. (2014) for high-redshift SMGs and low redshift ULIRGs (solid line with  $1\sigma$  spread indicated in dark grey) and the population of galaxies detected in H-ATLAS with  $z < 0.5$  (dashed line with  $1\sigma$  spread indicated in light grey).

sample size and large scatter on this measurement, our luminosities are overall consistent with both the HERUS and ALESS samples. The median effective temperature of the ALESS sample is  $T = 31 \pm 1$  K, which is consistent at the  $2\sigma$  level with that of the HERUS sample, for which  $T = 38 \pm 3$  K. The median dust temperature of our sample is significantly higher at  $T = 59 \pm 4$  K. The high dust temperatures can be interpreted as a product of the extreme SFRs present in our sample, though it is important to bear in mind that the significance of these results is likely explained by the combination of selection effects due to our observing of the brightest galaxies detected by Herschel and the sample of ALESS galaxies being selected at  $870 \mu\text{m}$ .

Fig. 5 shows the degree to which our sources exceed the ratio of the SFR (determined using the scaling relation of the far-IR luminosity given by Kennicutt & Evans 2012) to the dust mass. Given that our SFRs are derived from scaled far-IR luminosity, we can conclude that our sources have higher than expected luminosities for the amount of gas available for star formation. An obvious interpretation of this fact would be that a large fraction of the luminosity is due to an AGN, but without additional imaging we cannot confirm this. It is also important to note that this excess could be at least in part explained by selection bias, as we have chosen the brightest Herschel sources to follow up on. Additionally, degeneracies between our measures of SFR and dust mass, due to them being derived from the same photometry, could be causing us to overestimate the SFR (Santini et al. 2014).

Converting the rest-frame  $850 \mu\text{m}$  flux density of our sources to  $\text{H}_2$  gas mass (see Table 5) using the scaling relation given by Hughes et al. (2017), we find that our sources all lie on or above the mean relationship between SFR and  $\text{H}_2$  gas mass, as determined by Scoville et al. (2016). One interpretation is that our sources possess a higher star formation efficiency (SFE), provided that dust is an accurate tracer for molecular gas. Fitting a line parallel to the SMG/ULIRG relation shown in Fig. 5, and treating the range of dust masses as the  $1\sigma$  error, we find an increase in SFE by a factor of 6 when compared

with the value implied by the SMG/ULIRG relation from Rowlands et al. (2014). This increases to a factor of 50 when compared to the  $z < 0.5$  H-ATLAS galaxies.

Approximately 10 per cent of typical samples of SMGs have an associated AGN (Wang et al. 2013). Recent studies have shown that the comoving AGN luminosity density has a flatter profile than that of star formation at  $z > 1$  (Runburg et al. 2022). This implies that the relative importance of AGN contribution to luminosity is increasing at this epoch. An unknown fraction of our sources could have their SFR overestimated due to significant contamination in the infrared by strongly obscured AGN. As a simple test of this, we used the SED fitting code X-CIGALE (Yang et al. 2019a) to fit a model of dust emission based on Dale et al. (2014) and the AGN emission model from Fritz, Franceschini & Hatziminaoglou (2006). We allowed the for the full range of possible values to be explored in our AGN model, since we are lacking any observational constraints. However, we found that the inferred fraction of AGN IR luminosity,  $f_{\text{AGN}}$ , was strongly dependent on our model assumptions for star formation history (SFH). Since we are unable to constrain the SFHs of our sources, we are unable to provide a meaningful constraint on  $f_{\text{AGN}}$ . In order to quantify this effect, additional observational evidence would need to be considered. For example, the stellar mass could be estimated from broadband SED fitting. However, this procedure would either require careful lens light subtraction or additional follow-up observations in the X-ray hard band to reveal the obscured nucleus.

Out of our combined sample of 13 reconstructed sources, nine show signs of possessing a disturbed morphology, with at least two being potential mergers. Morphological studies of submm galaxies have found that it is common for them to exhibit peculiar and complex morphologies; this is suggestive of a high frequency of mergers in the population (Chapman et al. 2003; Ricciardelli et al. 2010). It has been found that samples of ULIRGs in the Cosmic Assembly Near-infrared Deep Extragalactic Legacy Survey (CANDELS; Grogin et al. 2011) fields are more likely to have undergone interactions and mergers than a field galaxy sample Kartaltepe et al. (2012). However, it has also been shown that the morphologies of a sample of spectroscopically confirmed SMGs do not differ significantly from a sample of star forming galaxies in the field Swinbank et al. (2010). Galaxy morphology is strongly correlated with SFH (Larson, Tinsley & Caldwell 1980; Strateva et al. 2001; Lee et al. 2013). At  $z \sim 3$ , massive galaxies are mostly star forming disks, with the SFR peaking at  $1 < z < 2$  (Madau & Dickinson 2014), and then dropping as the fraction of massive quiescent galaxies grows rapidly. This period of galaxy evolution is extremely dramatic, and many different mechanisms have been proposed to explain the build-up of ETGs we see today. Galaxy mergers are one such mechanism, as they are effective at disturbing the morphology and building a central bulge in a galaxy (Hopkins et al. 2006; Snyder et al. 2011). They have also been shown to trigger starbursts and AGNs, which can lead to strong supernovae and/or AGN winds contributing to the quenching of a galaxy (Bekki et al. 2005).

## 6 CONCLUSIONS

We have modelled seven ALMA observations of strongly lensed submillimetre galaxies. Four of these systems are galaxy-galaxy scale strong lenses, which are well described by a single power-law mass profile; the remaining three are group-scale lenses, which have been successfully fitted with two power-law mass profiles. Where we found it improved the fit, an external shear term was also included in the lens model. In this work, we have opted to model the visibility

data directly, rather than to work with CLEANed image plane data. Whilst the uv-plane method is more computationally expensive, it does not suffer from the image pixel covariances introduced due to incomplete sampling of the uv-plane. However, Dye et al. (2018) showed that with sufficient sampling of the uv-space, both the image-plane and direct visibility modelling approaches produce very similar results. We have fitted a smooth power-law density profile (and in some cases two profiles) to each of the lensing systems, and found that most of the lenses are close to isothermal. This result is expected in massive ETGs due to the combination of an inner Sérsic profile representing the baryonic component and an outer Navarro–Frenk–White (Navarro, Frenk & White 1996) profile representing the dark matter component (Lapi et al. 2012). In some instances, there are significant deviations from an isothermal power-law slope, which may be due to degeneracies between parameters in our model or reflect the true nature of the lens, but we leave a more thorough explanation of this to further work.

By obtaining the total magnification factors from our models, we have demagnified the available submillimetre source photometry. Fitting rest frame SEDs to these data allowed us to determine the dust temperatures, dust masses, intrinsic luminosities, and SFRs of our lensed sources. In order to estimate a range of possible dust masses for these sources, we fitted the photometry with both single temperature, optically thick SEDs, as well as dual temperature, optically thin SEDs. Using the midpoint of this range to calculate the SFR to dust mass ratio, we find that all seven of our sources lie above the mean ratio for the SMG/ULIRG population as described in Rowlands et al. (2014).

Our combined sample of strongly lensed submm galaxies contains a majority of sources that display a disturbed morphology. Nine of the 13 galaxies in our sample are visually classified as being disturbed, with at least two of them having evidence of being mergers (H-ATLAS J142935.3-002836, and H-ATLAS J083051.0+01322). Other observations of submm galaxies have found similarly high fractions of disturbed morphologies, such as those made by Chapman et al. (2004), who used high-resolution optical and radio imaging of 12 submm galaxies in order to study their spatially extended star formation activity. It has been suggested that high density molecular gas is more commonly found in galaxy mergers than quiescent systems, and that this can be used to predict the star formation mode of a galaxy (Papadopoulos & Geach 2012). We are not able to conclusively say what fraction of our sample’s disturbed morphologies are a result of mergers, but the source with the most extreme ratio of SFR and gas mass (H-ATLAS J083051.0+01322) does display a significantly disturbed morphology, and is identified as being a merger by Yang et al. (2019b).

## ACKNOWLEDGEMENTS

We thank the anonymous referee for their helpful comments and suggestions. JM acknowledges the support of the UK Science and Technology Facilities Council (STFC), and thanks John Shawcroft for their helpful comments on this manuscript. CF acknowledges financial support from CNPq (processes 433615/2018-4 e 314672/2020-6). JGN acknowledges the PGC 2018 project PGC2018-101948-B-I00 (MICINN/FEDER). MG acknowledges the support of the UK STFC. AL is partly supported by the PRIN MIUR 2017 prot.20173ML3WW 002 ‘Opening the ALMA window on the cosmic evolution of gas, stars, and massive black holes’, and by the EU H2020-MSCA-ITN-2019 project 860744 ‘BiD4BEST: Big Data applications for Black hole Evolution Studies’. JLW acknowledges

support from an STFC Ernest Rutherford Fellowship (ST/P004784/1 and ST/P004784/2).

This paper makes use of the following ALMA data: ADS/JAO.ALMA#2013.1.00358.S. ALMA is a partnership of ESO (representing its member states), NSF (USA) and NINS (Japan), together with NRC (Canada) and NSC and ASIAA (Taiwan) and KASI (Republic of Korea), in cooperation with the Republic of Chile. The Joint ALMA Observatory is operated by ESO, AUI/NRAO, and NAOJ.

*Herschel* is an ESA space observatory with science instruments provided by European-led Principal Investigator consortia and with important participation from NASA.

## DATA AVAILABILITY

The data underlying this article were accessed from the ALMA Science Archive, and are contained within the dataset ADS/JAO.ALMA#2013.1.00358.S. The derived data generated in this research will be shared on reasonable request to the corresponding author.

## REFERENCES

- Abolfathi B. et al., 2018, *ApJS*, 235, 42  
 Alaghband-Zadeh S. et al., 2012, *MNRAS*, 424, 2232  
 ALMA Partnership et al., 2015, *ApJ*, 808, L4  
 Amvrosiadis A. et al., 2018, *MNRAS*, 475, 4939  
 An F. X. et al., 2019, *ApJ*, 886, 48  
 Asboth V. et al., 2016, *MNRAS*, 462, 1989  
 Bakx T. J. L. C. et al., 2017, *MNRAS*, 473, 1751  
 Bekki K., Couch W. J., Shioya Y., Vazdekis A., 2005, *MNRAS*, 359, 949  
 Blain A. W., 1996, *MNRAS*, 283, 1340  
 Blain A. W., Smail I., Ivison R., Kneib J.-P., Frayer D. T., 2002, *Phys. Rep.*, 369, 111  
 Briggs D. S., 1995, PhD thesis, New Mexico Institute of Mining and Technology, United States  
 Bussmann R. S. et al., 2012, *ApJ*, 756, 134  
 Bussmann R. S. et al., 2013, *ApJ*, 779, 25  
 Bussmann R. S. et al., 2015, *ApJ*, 812, 43  
 Calanog J. A. et al., 2014, *ApJ*, 797, 138  
 Cañameras R. et al., 2015, *A&A*, 581, A105  
 Cañameras R. et al., 2017a, *A&A*, 600, L3  
 Cañameras R. et al., 2017b, *A&A*, 604, A117  
 Carlstrom J. E. et al., 2011, *PASP*, 123, 568  
 Casey C. M., Narayanan D., Cooray A., 2014, *Phys. Rep.*, 541, 45  
 Cava A., Schaerer D., Richard J., Pérez-González P. G., Dessauges-Zavadsky M., Mayer L., Tamburello V., 2018, *Nature Astron.*, 2, 76  
 Chapman S. C., Windhorst R., Odewahn S., Yan H., Conselice C., 2003, *ApJ*, 599, 92  
 Chapman S. C., Smail I., Windhorst R., Muxlow T., Ivison R. J., 2004, *ApJ*, 611, 732  
 Clements D. L. et al., 2017, *MNRAS*, 475, 2097  
 Dale D. A., Helou G., Magdis G. E., Armus L., Díaz-Santos T., Shi Y., 2014, *ApJ*, 784, 83  
 Dessauges-Zavadsky M. et al., 2019, *Nature Astron.*, 3, 1115  
 Dudzeviciute U. et al., 2020, *MNRAS*, 494, 3828  
 Dunne L. et al., 2011, *MNRAS*, 417, 1510  
 Dunne L., Eales S., Edmunds M., Ivison R., Alexander P., Clements D. L., 2000, *MNRAS*, 315, 115  
 Dye S. et al., 2014, *MNRAS*, 440, 2013  
 Dye S. et al., 2015, *MNRAS*, 452, 2258  
 Dye S. et al., 2018, *MNRAS*, 476, 4383  
 Dye S. et al., 2022, *MNRAS*, 510, 3734  
 Eales S. et al., 2010, *PASP*, 122, 499  
 Farrah D. et al., 2013, *ApJ*, 776, 38

- Fritz J., Franceschini A., Hatziminaoglou E., 2006, *MNRAS*, 366, 767
- Griffin M. J. et al., 2010, *A&A*, 518, L3
- Grogin N. A. et al., 2011, *ApJS*, 197, 35
- Guo Q., White S. D. M., 2008, *MNRAS*, 384, 2
- Harrington K. C. et al., 2021, *ApJ*, 908, 95
- Hopkins P. F., Hernquist L., Cox T. J., Matteo T. D., Robertson B., Springel V., 2006, *Astrophys. J. Suppl. Ser.*, 163, 1
- Hughes T. M. et al., 2017, *MNRAS*, 468, L103
- Inoue K. T., Minezaki T., Matsushita S., Chiba M., 2016, *MNRAS*, 457, 2936
- James A., Dunne L., Eales S., Edmunds M. G., 2002, *MNRAS*, 335, 753
- Kartaltepe J. S. et al., 2012, *ApJ*, 757, 23
- Keeton C. R., 2001, preprint ([astro-ph/0102341](https://arxiv.org/abs/astro-ph/0102341))
- Kennicutt R. C., Evans N. J., 2012, *ARA&A*, 50, 531
- Kroupa P., 2001, *MNRAS*, 322, 231
- Lapi A. et al., 2011, *ApJ*, 742, 24
- Lapi A. et al., 2018, *ApJ*, 857, 22
- Lapi A., Negrello M., González-Nuevo J., Cai Z. Y., De Zotti G., Danese L., 2012, *ApJ*, 755, 46
- Larson R. B., Tinsley B. M., Caldwell C. N., 1980, *ApJ*, 237, 692
- Lee B. et al., 2013, *ApJ*, 774, 47
- Mackenzie T. et al., 2011, *MNRAS*, 415, 1950
- Madau P., Dickinson M., 2014, *ARA&A*, 52, 415
- McMullin J. P., Waters B., Schiebel D., Young W., Golap K., 2007, in Shaw R. A., Hill F., Bell D. J., eds, *ASP Conf. Ser. Vol. 376, Astronomical Data Analysis Software and Systems XVI*. Astron. Soc. Pac., San Francisco, p. 127
- Navarro J. F., Frenk C. S., White S. D. M., 1996, *ApJ*, 462, 563
- Nayyeri H. et al., 2016, *ApJ*, 823, 17
- Negrello M. et al., 2010, *Science*, 330, 800
- Negrello M. et al., 2014, *MNRAS*, 440, 1999
- Negrello M. et al., 2017, *MNRAS*, 465, 3558
- Negrello M., Perrotta F., González-Nuevo J., Silva L., de Zotti G., Granato G. L., Baccigalupi C., Danese L., 2007, *MNRAS*, 377, 1557
- Nightingale J. W. et al., 2021, *J. Open Sour. Softw.*, 6, 2825
- Nightingale J. W., Dye S., 2015, *MNRAS*, 452, 2940
- Nightingale J. W., Dye S., Massey R. J., 2018, *MNRAS*, 478, 4738
- Okido D. H., Furlanetto C., Trevisan M., Tergolina M., 2020, *Proc. Int. Astron. Union*, 15, 188
- Oliver S. J. et al., 2012, *MNRAS*, 424, 1614
- Oogi T., Habe A., 2012, *MNRAS*, 428, 641
- Papadopoulos P. P., Geach J. E., 2012, *ApJ*, 757, 157
- Perrotta F., Magliocchetti M., Baccigalupi C., Bartelmann M., De Zotti G., Granato G. L., Silva L., Danese L., 2003, *MNRAS*, 338, 623
- Pilbratt G. L. et al., 2010, *A&A*, 518, L1
- Planck Collaboration et al., 2016, *A&A*, 594, A13
- Poglitsch A. et al., 2010, *A&A*, 518, L2
- Powell D., Vegetti S., McKean J. P., Spingola C., Rizzo F., Stacey H. R., 2020, *MNRAS*, 501, 515
- Puglisi A. et al., 2019, *ApJ*, 877, L23
- Ricciardelli E., Trujillo I., Buitrago F., Conselice C. J., 2010, *MNRAS*, 406, 230
- Riechers D. A. et al., 2013, *Nature*, 496, 329
- Riechers D. A., Cooray A., Pérez-Fournon I., Neri R., 2021, *ApJ*, 913, 141
- Rowlands K. et al., 2014, *MNRAS*, 441, 1017
- Runburg J. et al., 2022, *ApJ*, 924, 133
- Rybak M., McKean J. P., Vegetti S., Andreani P., White S. D. M., 2015a, *MNRAS*, 451, L40
- Rybak M., Vegetti S., McKean J. P., Andreani P., White S. D. M., 2015b, *MNRAS*, 453, L26
- Santini P. et al., 2014, *A&A*, 562, A30
- Scoville N. et al., 2016, *ApJ*, 820, 83
- Shirley R. et al., 2021, *MNRAS*, 507, 129
- Simpson J. M. et al., 2014, *ApJ*, 788, 125
- Smith D. J. B. et al., 2013, *MNRAS*, 436, 2435
- Snyder G. F., Cox T. J., Hayward C. C., Hernquist L., Jonsson P., 2011, *ApJ*, 741, 77
- Speagle J. S., 2020, *MNRAS*, 493, 3132
- Spilker J. S. et al., 2016, *ApJ*, 826, 112
- Strateva I. et al., 2001, *AJ*, 122, 1861
- Sun F. et al., 2021, *ApJ*, 908, 192
- Suyu S. H., 2012, *MNRAS*, 426, 868
- Suyu S. H., Marshall P. J., Hobson M. P., Blandford R. D., 2006, *MNRAS*, 371, 983
- Swinbank A. M. et al., 2010, *MNRAS*, 405, 234
- Swinbank A. M. et al., 2013, *MNRAS*, 438, 1267
- Tadaki K.-i. et al., 2020, *ApJ*, 901, 74
- Tergolina M., 2020, Master's thesis, Federal University of Rio Grande do Sul
- Toft S. et al., 2014, *ApJ*, 782, 68
- Turner E. L., Ostriker J. P., Gott J. R. I., 1984, *ApJ*, 284, 1
- Viero M. P. et al., 2014, *ApJS*, 210, 22
- Wang R. et al., 2007, *AJ*, 134, 617
- Wang S. X. et al., 2013, *ApJ*, 778, 179
- Warren S. J., Dye S., 2003, *ApJ*, 590, 673
- Wootten A., Thompson A. R., 2009, *Proc. IEEE*, 97, 1463
- Yang G. et al., 2019a, *MNRAS*, 491, 740
- Yang C. et al., 2019b, *A&A*, 624, A138
- Zhang Z.-Y. et al., 2018, *MNRAS*, 481, 59

This paper has been typeset from a  $\text{\TeX}/\text{\LaTeX}$  file prepared by the author.